Journal of Molecular Structure: THEOCHEM xxx (2010) xxx–xxx

Contents lists available at ScienceDirect

Journal of Molecular Structure: THEOCHEM

journal homepage: www.elsevier.com/locate/theochem

Electron and vibrational spectroscopies using DFT, plane waves and pseudopotentials: CASTEP implementation

V. Milman [a,*], K. Refson [b], S.J. Clark [c], C.J. Pickard [d], J.R. Yates [e], S.-P. Gao [f], P.J. Hasnip [g], M.I.J. Probert [g], A. Perlov [a], M.D. Segall [h]

[a] Accelrys, 334 Science Park, Cambridge CB4 0WN, UK
[b] Rutherford Appleton Laboratory, Chilton, Didcot, Oxfordshire OX11 0QX, UK
[c] Department of Physics, University of Durham, South Road, Durham DH1 3LE, UK
[d] Department of Physics and Astronomy, University College London, Gower Street, London WC1E 6BT, UK
[e] Department of Materials, University of Oxford, Parks Road, Oxford OX1 3PH, UK
[f] Department of Materials Science, Fudan University, Shanghai 200433, People's Republic of China
[g] Department of Physics, University of York, York YO10 5DD, UK
[h] Cavendish Laboratory, University of Cambridge, Cambridge CB3 0HE, UK

ARTICLE INFO

Article history:
Received 23 November 2009
Accepted 21 December 2009
Available online xxxx

Keywords:
Density functional theory
Electron energy loss spectroscopy
Raman spectroscopy
Nonlinear optical materials

ABSTRACT

Density functional theory can be used to interpret and predict spectroscopic properties of solid-state materials. The relevant computational solutions are usually available in disparate DFT codes, so that it is difficult to use a consistent approach for analyzing various spectroscopic features of a given material. We review the latest developments that are aimed to provide a collection of analytical tools within one DFT package, CASTEP. The applications covered include core-level EELS, solid-state NMR, optical properties, IR and Raman spectroscopy. We present also results of the EELS analysis of NbO and Nb_2O_5 that show the first published example of CASTEP spectra from d-states. Raman activities calculated for a test set of small molecules and the convergence requirements for such calculations are discussed.

1. Introduction

Developments in electronic structure methods, in particular in density functional theory (DFT), combine with the continuous increase of available computing capacities to deliver unprecedented power to computational experiments on an atomistic level. The accuracy and robustness of DFT makes this technique the method of choice in assisting the design and development of the next generation of devices for nanoscale applications [1]. The underlying principle of DFT is that the total energy of the system is a unique functional of the electron density, hence it is natural that there exist a large number of computer programs that are designed for calculations of the total energy and its derivatives such as atomic forces and the stress tensor. These tools became invaluable in the field of Computational Crystallography since they allow the application of quantum mechanics for structure prediction, study of chemical bonding, mechanical properties, and lattice dynamics [2]. An important advantage of theoretical methods is the ability to carry out investigations of condensed phases under extreme conditions of high pressures and temperatures [3]. Such applications open the possibility of studying materials under multi-TPa compression that might exist in the core of massive exoplanets [4].

Energy and related properties, including the force constants that define the lattice dynamics of a crystal, are the ground-state properties and hence the natural products of a DFT calculation. The situation is less straightforward when DFT is applied to the studies of electronic properties of materials. The accuracy of DFT results for properties that involve excitations is more questionable, and often more sophisticated approaches are required to evaluate the response of a solid to an external time-dependent perturbation such as electric or magnetic field. Excited state calculations, however, are vitally important for evaluation of e.g. optical properties (dielectric function, reflectivity, absorption, and refractive index) and polarizabilities. These properties enable researchers to calculate various spectra that can provide a fingerprint of a particular structure as required for example for phase identification; alternatively this route potentially leads to a discovery of new materials with desired properties, such as a high second harmonic generation coefficient. This direction of "Computational Spectroscopy" has a long history, but traditionally it has been developed mostly in connection with properties of isolated molecules. Recent advances in theoretical spectroscopy [5] are largely based on the techniques that go beyond the ground-state DFT methodology,

* Corresponding author. Tel.: +44 1223 228619; fax: +44 1223 228501.
E-mail address: vmilman@accelrys.com (V. Milman).

0166-1280/$ - see front matter © 2010 Elsevier B.V. All rights reserved.
doi:10.1016/j.theochem.2009.12.040

by using for example time-dependent DFT or many-body perturbation theory.

The situation that requires different methods for computational studies of structures and of spectroscopic properties is not completely satisfactory; it is highly desirable to use a consistent approach to predict both the structure and properties of a material. Such calculations should be accessible in terms of computational cost to a wide community of researchers, a requirement satisfied by DFT methods. The accuracy of spectra calculated using DFT is often sufficient to carry out qualitative or even quantitative studies, thus it is tempting to accept the DFT level of description until it is proven to be insufficiently accurate for a certain system or property.

The present article presents a review of recent DFT applications to spectroscopic problems based on a specific computer code, CASTEP [6,7]. CASTEP uses the plane-wave pseudopotential method to solve one-electron Kohn–Sham equations. The wavefunctions are expanded in a plane-wave basis set defined by the use of periodic boundary conditions and Bloch's theorem. The electron–ion potential is described by means of *ab initio* pseudopotentials within either norm-conserving [8] or ultrasoft [9] formulations. Direct energy minimization schemes are used to obtain, self-consistently, the Kohn–Sham wavefunctions and corresponding charge density. In particular the conjugate gradient [10] and density mixing [11,12] schemes are implemented. The robust electron ensemble DFT approach can be used for systems with partial occupancies (in particular, metals) [6,13]. The convergence of the calculations is controlled essentially by just two parameters, namely the size of the basis set which is defined by the energy cut-off for plane waves, and the accuracy of the Brillouin zone integration as determined by the number of special *k*-points used for sampling.

CASTEP has been used successfully to study structures, mechanical properties, and phase stability of inorganic materials. Applications of this total energy based approach to the prediction and interpretation of spectroscopic properties are less well publicized. This article reviews calculations of core-level electron energy loss (EELS) spectra, vibrational IR and Raman spectra, NMR chemical shifts, linear and nonlinear optical spectra. The goal is to illustrate the level of accuracy attainable in a consistent fashion by using the same atomistic modelling tools for all parts of a scientific investigation.

2. Electron energy loss spectroscopy

Spectroscopic techniques that explore transitions from or to core-level orbitals, such as electron energy loss spectroscopy, offer a popular experimental probe to investigate properties of materials, nanostructures, and biological molecules. There are several versions of EELS, and among them EELS associated with electron microscopy is especially popular for material characterization. Theoretical calculations offer a complementary tool to the experimental core-level spectroscopy.

Core-level spectroscopy within plane-wave pseudopotential approach is not straightforward since the all-electron wave function inside the core region is required for the matrix element calculations. Furthermore, an important consideration in EELS modelling is the inclusion of the core–hole effect in calculations. Core orbitals are not considered explicitly in pseudopotential methods such as that used in CASTEP; hence a special approach is required. The formalism of EELS within the CASTEP framework has been developed by Pickard et al. [14–16], and the initial papers calculated K-edge spectra of diamond and cubic boron nitride in good agreement with experimental measurements [17]. There are two key elements to the CASTEP implementation. Firstly, a projector augmented wave (PAW) reconstruction of the wavefunction inside the core region is required to obtain an accurate matrix element. Secondly, the on-the-fly generation of ultrasoft pseudopotentials is used to generate an excited pseudopotential "on demand" as required to study the core–hole effect [18].

Early applications of EELS modelling using plane-wave pseudopotential method by Gao et al. included calculations of K-edges in a number of materials including group-III nitrides [19], carbon and boron nitride polymorphs [20], and CaB_6 [21]. Good agreement with experiment has been achieved and theoretical core-level spectra were used successfully in interpreting experimental spectra, predicating theoretical reference spectra when reliable experimental spectra were not available, identifying correlations between EELS spectra and crystal structure, and estimating the reliability of experimental spectra. The most recent CASTEP implementation of the PAW reconstruction technique has been described in [18], showing good agreement for K-edge results in such materials as LiF, BeO, cubic BN, CaB_6, MgB_2, SiC, diamond, and C_3N_4.

Extensive tests of CASTEP EELS functionality were undertaken by way of comparing calculated results to reported all-electron data from WIEN2k [22] calculations as well as to the experimental results. Gao et al. [23] calculated spectra for such disparate materials as MgO (Mg K-edge), Si (K-edge and L_2 edge), NiSi and Ni_2Si (Ni and Si L_2 edge), TiN (N K-edge), cubic and hexagonal BN (B and N K-edge), hexagonal GaN (N K-edge). These calculations showed that the inclusion of core–hole effects even on the DFT level of theory usually improves agreement with experiment, sometimes dramatically as in cubic BN. Calculations with a core hole can be more expensive computationally since it is desirable to introduce a core hole in a supercell so that the distance between unphysical periodic images is at least 8–10 Å. This additional cost should be balanced against more accurate spectra interpretation, especially in the region of the threshold. Calculated spectra faithfully reproduce the observed dependence of EELS signal on the electric field polarization direction in hexagonal structures of BN and GaN [19,23].

There are numerous examples where experimental EELS spectra are used as a fingerprint for subsequent phase identification in complex multi-phase materials. One such example refers to the promising family of biomaterials, so-called biphasic calcium phosphates. The two materials in question are β-tricalcium phosphate (β-TCP) and hydroxyapatite. CASTEP calculations [23] were able to explain the difference between the fine structure of O K-edge in these two materials as being due to the lower symmetry of the β-TCP structure compared to hydroxyapatite. The calculated signal from ten inequivalent atoms in the β-TCP structure had to be added together with a chemical shift determined by the differences in the total energies; this convolution produces a smooth featureless spectrum. PO_4 groups in hydroxyapatite have only three inequivalent oxygen atoms, and the convolution preserves some structural features in the low energy part of the spectrum. The interpretation put forward in the experimental study involved the signal from the disordered OH group in hydroxyapatite [24], while CASTEP results showed that the OH signal lies in a different part of the spectrum and does not contribute to the observed fingerprint.

CASTEP EELS analysis has been applied recently to the O K-edge of metal oxides with the fluorite structure, namely zirconia, ceria and urania [25]. Good agreement with experimental results was achieved, especially when core holes were included and a GGA + U treatment [26] applied to the strongly correlated UO_2 system. Another transition metal–metalloid system studied recently with CASTEP is ZrC [27] where the C K-edge was calculated and found to agree well with the experimental spectrum.

Care should be taken when applying DFT tools to calculate the fine structure of EELS edges. A detailed methodological study based

Please cite this article in press as: V. Milman et al., J. Mol. Struct. (THEOCHEM) (2010), doi:10.1016/j.theochem.2009.12.040

on CASTEP and WIEN2k codes provides step by step illustrations that allow one to obtain results well converged with respect to the basis set size, k-point sampling and the supercell size, as illustrated by the example calculations of the Al K-edge in metallic aluminium and in hexagonal AlN [28].

CASTEP simulations can be used to establish reliable peak positions that can be combined with the energy-filtered transmission electron microscopy to achieve a sub-nanometre particle mapping. An example application used CASTEP to establish if the measured peak corresponded to a collective or single electron excitation. The results allowed to separate the yttrium $N_{2,3}$ signal from cubic or monoclinic phases from the plasmon peaks [29]. This signal was subsequently used for the first chemical mapping of sub-nanometre particles of oxide dispersion strengthened FeCr alloys.

A recent example of the experimental search for EELS fingerprint is the study of two members of the complex niobium–oxygen system, namely niobium monoxide (NbO) and niobium pentoxide (Nb_2O_5). Niobium oxide is a promising material for high-capacity solid electrolyte capacitors. Unfortunately, niobium-based capacitors contain a mixture of phases, and display high leakage current due to the presence of the conducting NbO phase. EELS spectra of NbO and Nb_2O_5 were shown to have clearly different near-edge fine structure, and hence EELS spectroscopy was suggested as an analytical technique of choice to analyse and control phase content of Nb–O based materials [30,31]. We used this system to validate CASTEP results for a transition metal EELS edge by calculating Nb M_{45} and Nb M_{23} edges in addition to the O K-edge.

The calculations were performed for the experimentally observed structures of NbO and Nb_2O_5. NbO crystallizes in the defective rock-salt structure with 25% ordered vacancies both in the niobium and in the oxygen sublattice. Its structure can be described by the space group $Pm\bar{3}m$ (no. 221), with the lattice parameter of 4.2103 Å [32]. Nb_2O_5 appears as an amorphous phase or in several complex crystalline modifications. Experimental EELS study was carried out on a monoclinic cell belonging to the space group $P2$ [32]. We chose a slightly less complex modification, namely the tetragonal phase in the space group $I4/mmm$ (no. 139) with lattice parameters $a = 20.44$ Å and $c = 3.832$ Å [33]. We used PBE exchange–correlation functional [34], ultrasoft pseudopotentials generated on the fly, and the energy cut-off of 610 eV.

A core hole was created on every symmetry inequivalent atom in the unit cell, one at a time (there is one Nb and one O inequivalent atom in NbO, three Nb and seven O inequivalent atoms in Nb_2O_5). This process generates one structure of NbO for each edge to be studied, and either three (for Nb edges) or seven (for O edge) structures of Nb_2O_5, each containing exactly one core hole. Core holes were introduced on Nb 3d, Nb 3p, and O 1s levels for simulations of Nb M_{45}, Nb M_{23}, and O K edges, respectively. A supercell is created for each structure; the size of the cell was $2 \times 2 \times 2$ for cubic NbO, and $1 \times 1 \times 2$ for tetragonal Nb_2O_5. The next step is to find the symmetry of a structure with a core hole; the use of symmetry speeds up calculations by reducing the number of k-points to consider. NbO supercells have the tetragonal $P4/mmm$ symmetry and contain 48 atoms; Nb_2O_5 supercells are either monoclinic, space group Cm, or triclinic, space group $P1$, in either case containing 112 atoms. We used a $3 \times 3 \times 3$ Monkhorst–Pack grid for Brillouin zone sampling in NbO supercells, and $1 \times 1 \times 3$ grid in Nb_2O_5. These grids correspond approximately to the distance of 0.04 $Å^{-1}$ between the sampling points.

EELS edges from each atom with a core hole were calculated using the formalism described in [23]. The simulation of Nb_2O_5 spectra is more involved since there are a number of inequivalent atoms in the crystal structure. We applied the chemical shift determined by the difference in total energies to each spectrum, and summed them up taking into account degeneracies of inequivalent Wyckoff sites. The edges that contain spin–orbit splitting (Nb M_{23} and M_{45} edges) contain both components in the experimental data; we simulated this effect by using experimental values of differences between electron binding energies: 15.5 eV for Nb M_{23} and 2.7 eV for Nb M_{45} edge [35]. Finally, we applied Gaussian instrumental broadening of 2.1 eV, the value reported in the experimental study [30]. We also applied Lorentzian broadening due to the core-level lifetime and to the excited state lifetime; the width due to the latter effect was modelled with an empirical linear function $\Gamma(E) = 0.1E$, where E is the energy above the threshold [22].

The results are presented in Fig. 1. Calculated spectra are aligned with experimental ones using the position of the first peak as a guide. There is a good quantitative agreement between the results of CASTEP calculations and the experimental spectra, both for peak positions and relative intensities. Nb M_{45} edge in NbO has a shoulder and a bump (Fig. 1a), while there is very wide plateau in Nb_2O_5 (Fig. 1b). Nb M_{23} edge in NbO is featureless; the two peaks in Fig. 1c are due to spin–orbit splitting (Fig. 1c). The same edge in Nb_2O_5 possesses a well defined shoulder (Fig. 1d). The shoulder in the calculated O K-edge for NbO corresponds to the experimentally observed double peak [30]; the two characteristic features at higher energies are also reproduced well. In summary, these results support the suggestion that Nb M_{45} edge as well as Nb M_{23} edge and O K-edge can be used for quantitative phase analysis of the mixture of niobium monoxide and pentoxide.

3. NMR calculations

Solid-state NMR is a rapidly evolving technique which is used increasingly to obtain information about complex crystalline structures including inorganic materials with strong covalent and ionic bonding, and more weakly bound molecular crystals [36]. As the technique becomes more widely used and applied to more challenging systems, modelling plays an increasingly important role in interpreting experimental data.

It has recently been shown how to calculate NMR chemical shifts in both molecules and solids within DFT and using pseudopotentials to describe the core–valence interactions [37,38]. The approach is based on gauge including projector augmented waves (GIPAW), derived from the PAW electronic structure method and implemented in CASTEP. The calculated chemical shifts are typically accurate to a few percent of the measured shift range. The GIPAW approach is a general method for the prediction of magnetic response properties, and it has also been applied to the prediction of electron paramagnetic resonance (EPR) g-tensors of defects in silica [39]. The early applications of the GIPAW approach reviewed in [6] included, for example, the study of the atomic structure of icosahedral boron carbide, where both X-ray and neutron techniques had failed to locate the carbon atoms in the B_4C structure [40]. In another application both the chemical shifts and the quadrupolar coupling constants for ^{17}O were calculated for a variety of SiO_2 polymorphs [41]. The calculated NMR parameters of cristobalite, quartz, coesite, and faujasite were found to be in excellent agreement with experimental data, and formed the basis of the first assignment of the spectrum of ferrierite [41].

3.1. Organic molecular crystals

A good review of CASTEP calculations of NMR properties of molecular organic compounds has been given in [42]. A target for the NMR computations is to bring the error in calculated ^{13}C chemical shifts to within 2 ppm. This is a challenging task, and one of the relevant questions is when one can expect accurate DFT answers. It appears that, for example, a comparison of different polymorphs is a promising area, where calculations can be used to understand the role of crystal packing. There is a number of open issues related to

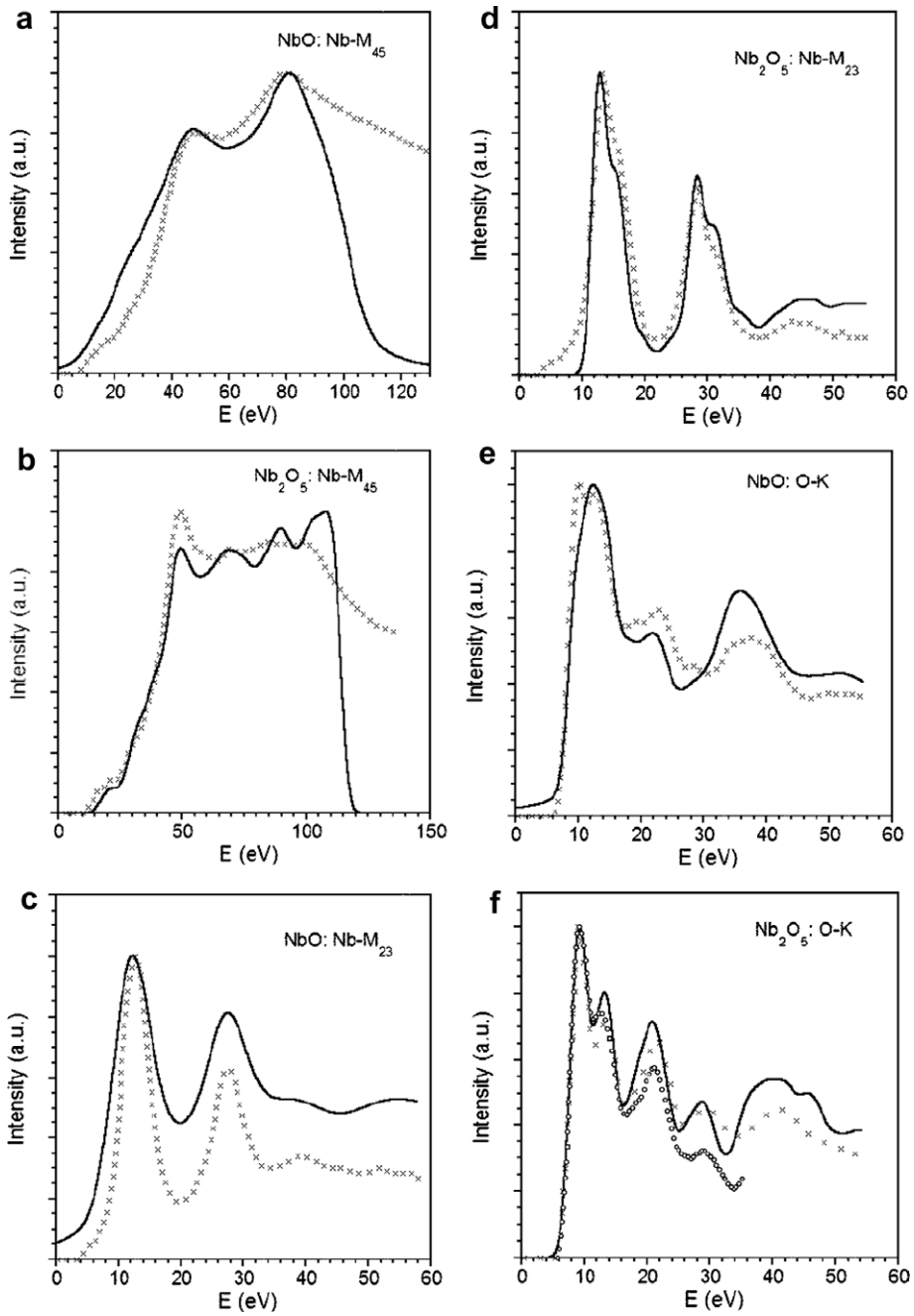

Fig. 1. EELS spectra showing the Nb M_{45} (a and b) and M_{23} (c and d) edges and the O K-edge (e and f) for NbO (a, c, e) and Nb_2O_5 (b, d, f) crystals. Solid line – theory, crosses [30] and circles [31].

the design of a good theoretical protocol, e.g. which exchange–correlation functional to use, whether to optimize atomic positions or to use experimental geometry (possibly with optimization of protons), whether to fix to unity the slope of experiment vs theory plots when calculating the reference shift. The results analysed in [42] show the promise of CASTEP calculations for such materials as flurbiprofen, finasteride, terbutaline sulfate, testosterone, ampicillin, maltose, etc. We provide below a brief summary of more recent results that provide better understanding of the role and accuracy of GIPAW calculations in structure analysis and prediction.

CASTEP NMR calculations have been carried out for 14 organic crystals by Johnston [43], and the results were shown to reproduce experimental data better than the calculations on isolated molecules that do not take into account crystal packing or hydrogen bonding effects. The difference is especially pronounced for carbohydrates, where the CASTEP RMS error relative to experiment was only 1.88 ppm, while the results for aromatic compounds show the RMS deviation of 3.05 ppm.

A comparative study of molecular crystal NMR using a solid-state approach (CASTEP) and a molecular approach (either CASTEP using a vacuum supercell approach, or a localised orbitals code such as Gaussian03) is a popular application since it allows one to judge the importance of crystal packing effects and the role of intermolecular shielding. For example, the study of ^{17}O chemical shifts and quadrupolar constants for two representative α-keto acids, sodium and lithium pyruvates, showed that solid-state CASTEP calculations gave much better agreement with the experimental data than those using a molecular cluster approach [44].

Please cite this article in press as: V. Milman et al., J. Mol. Struct. (THEOCHEM) (2010), doi:10.1016/j.theochem.2009.12.040

A comparison between molecular and solid-state calculations has been used to quantify the ring current effects caused by neighbouring molecules, as well as the role of hydrogen bonding. An earlier study of this type showed that in maltose anomers the change in the ^{1}H chemical shift can be used as a quantitative measure of intermolecular CH...O hydrogen bonding; the results accurately reproduce the two-dimensional ^{1}H–^{13}C MAS-J-HMQC solid-state NMR spectra [45]. This work was subsequently extended for uracil and 4-cyano-4′-ethynylbiphenyl, where a methodology was suggested for separating the hydrogen bonding and ring current effects on chemical shifts [46].

Another example of the importance of taking account of periodic boundary conditions is given in the extensive study of the ^{13}C chemical shift in a large group of amino acids and peptides, such as asparagines, glutamine, and glutamic acid [47]. The incorporation of lattice effects via periodic calculations that use optimized crystal geometries gives chemical shifts with a typical deviation from experiment in the 1–2 ppm range. The same conclusion has been made in the study of the ^{13}C chemical shift in vascular-selective drugs felodipine and amlodipine, where the use of GIPAW compared to the GIAO molecular method reduced the RMS error by a factor of two [48].

CASTEP results can be used as a basis for modelling of the results of sophisticated techniques such as two-dimensional double-quantum MAS NMR. This approach was applied to the study of the dipeptide β-AspAla [49]. CASTEP ^{1}H isotropic chemical shifts were shown to agree with experiment to better than 1 ppm, and hence the anisotropic component was subsequently used as a basis for multi-spin density-matrix simulation of double-quantum coherence experiment.

NMR measurements and calculations can provide more information than chemical shifts; for example, integer spin NMR has been used recently to investigate quadrupolar coupling parameters and EFG tensor asymmetry parameters for the ^{14}N nucleus in α-glycine, L-leucine and L-proline [50]. CASTEP results were used to assign parameters to correct sites and to orient the EFG tensors in the molecular frames; once the proton positions have been optimized, the calculations reproduce the EFG parameters much more accurately than non-periodic Gaussian calculations.

It is possible to use NMR chemical shifts, in addition with other characteristic signals, as part of the design of materials with requested properties. Filhol et al. [51] studied model polydiacetylenes with the aim of relating changes of optical properties to the twist of lateral groups. Chemical shifts as a function of such twists were shown to follow the known trend for blue/red isomerism of these compounds, which opens the way to building a statistical correlation between the two properties.

NMR calculations can be used in combination with experimental data as a way of structure determination of powdered solids. A methodology that uses proton spin-diffusion data, DFT geometry optimizations as well as calculations of ^{1}H and ^{13}C chemical shifts has been applied to the case of the small drug molecule thymol [52]. The method shows that CASTEP chemical shifts can match experimental ones to within 0.5 ppm for ^{1}H and within 2 ppm for ^{13}C, and the resultant crystal structure differs from the single-crystal X-ray diffraction result by only 0.07 Å.

The structure solution of cyameluric acid has become possible 150 years since it was first synthesized, and this success was due to the combination of solid-state NMR spectroscopy, DFT modelling and direct-space X-ray powder refinement techniques [53]. The process involved identification of the correct tautomer based on the comparison of experimental and calculated NMR spectra, followed by the crystal structure Pawley and Rietveld refinement based on the molecule optimized with CASTEP. Finally, hydrogen positions were refined by analysing NMR chemical shifts; the anisotropy of the chemical shift and the asymmetry parameter of the carbonyl ^{13}C were found to be good indicators of the hydrogen bonding environment.

A different application in solving crystal structure of an organic compound used ^{13}C and ^{15}N NMR spectroscopy as part of the investigation of polythiocyanogen, SCN [54]. A number of random periodic structures were generated and optimized, and the NMR spectra of the lowest energy candidates were analyzed. The combined analysis of crystal energies and NMR chemical shifts allowed the authors to suggest the most likely structure of the polymer.

Calculations of solid-state NMR parameters within the GIPAW formalism have made important contributions to solving crystal structures of such compounds as polymorphs of terbutaline sulfate using ^{13}C and ^{1}H NMR [55], or to investigation of the monomer–dimer equilibrium of zinc dialkyldithiophosphates from ^{31}P NMR [56].

An important methodological point refers to the role of thermal effects. Standard CASTEP calculations are carried out in the athermal limit, and hence there is always an uncertainty regarding the role of temperature. An investigation of the role of motional effects has been carried out for two organic solids, the amino acid L-alanine and a dipeptide, β-L-aspartyl-L-alanine [57]. Two methods were applied, one based on the zero-point correction from vibrational calculations and another based on averaging of the results over snapshots of an *ab initio* molecular dynamics simulation. The correction can be significant, of the order of few ppm, and the zero-point method was shown to be sufficiently reliable to be applied routinely when accurate estimates of chemical shifts are required.

The "thermal ellipsoids" associated with the structural uncertainties caused by the thermal motion of atoms might in fact be masking a small scale structural disorder. A recent study of bisphosphinoamine introduced a complex computational protocol aimed at evaluating effects of thermal motion on the ^{31}P NMR shift [58]. 2D correlation landscapes together with the calculated NMR shifts for structures with frozen-in vibrational modes were used to identify the presence of small amplitude structural disorder in addition to the thermal broadening of the peaks.

3.2. Carbon single-walled nanotubes (SWNTs)

An interesting group of molecular objects that have been studied using CASTEP NMR are carbon nanotubes [59–64]. These studies have a potential for underpinning the use of solid-state ^{13}C NMR for characterizing single-walled nanotubes. Calculations on a family of semiconducting zigzag (n, 0) SWNTs with n from 7 to 17 showed chemical shifts of up to 20 nm, with the chemical shift that decreases roughly inversely proportional to the tube's diameter [63]. This trend can be further subdivided by considering separately two main groups of SWNTS, namely semiconducting ($n = 3k$) and semimetallic ($n = 3k + 1$, where $l = 1$ or $l = 2$) [63,64]. The semimetallic nanotubes have a stronger isotropic diamagnetic shielding and hence have a smaller chemical shift for small-diameter SWNTs, less than about 15 Å. Interestingly, the chirality of a nanotube seems to have little impact on this conclusion [64].

Additional information can be obtained from ^{13}C and ^{1}H NMR chemical shifts for functionalized nanotubes. Attachment of typical groups such as NH, NCH_3, NCH_2OH, and CH_2–$NHCH_2$ to (7, 0), (8, 0), (9, 0), and (10, 0) single-walled carbon nanotubes has a clear signature in NMR spectra. The shifts were shown to be sensitive to the nature of the bond which is being functionalized and might be used therefore to characterize the structural details of the functionalized complexes [59].

NH-functionalized (n, 0) SWNTs with n = 11, 13–17 [60] showed a strong dependence of the chemical shift on the C–C distance and hence on the SWNT diameter, showing potential promise in determining diameter distribution of functionalized SWNTs. Another important aspect of SWNTs is the potential presence of defects,

either vacancies or packing imperfections. Stone–Wales or the 5/7/7/5 defect is considered to be the lowest energy defect in a SWNT; its NMR signature in (7, 0), (8, 0), (9, 0), and (10, 0) zigzag nanotubes has been studied in detail [61]. For the atoms that are part of the defect site, large chemical shifts are predicted (up to 150–160 ppm). For systems with high concentrations of SW defects it may be possible to identify the defects by these characteristically high shifts, provided that they are not obscured by shifts arising from metallic species.

CASTEP GIPAW calculations have been used to show that in some functionalized SWNTs there is little effect on NMR shifts of functionalized atoms. Fluorinated SWNTs offer the most clear example where no significant change of the chemical shift of carbon atoms involved in C–F bonding was found for systems with different functionalization patterns and degrees of fluorination; SWNT diameter also has little effect on this shift [62]. It appears that the local environment of fluorinated carbon atoms is largely independent of SWNT structural parameters which explains the lack of sensitivity in the chemical shift.

3.3. Inorganic solids

Solid-state NMR calculations are being applied to increasingly more complex and challenging studies in the area of inorganic materials as witnessed by some of the recently published results. One of the significant differences to the field of organic materials is a much wider variety of the nuclei used for solid-state characterization, many of them possessing a large electric quadrupole moment which makes accurate measurements challenging. A combination of modelling with experiment is aimed at improving resolution and sensitivity leading eventually to resolving the structures and solving important problems in materials science, chemistry, geochemistry, etc.

DFT calculations were used to interpret solid-state ^{89}Y MAS NMR spectra of $Y_2Ti_{2-x}Sn_xO_7$ pyrochlores, materials with applications for the encapsulation of actinide-bearing radioactive waste [65]. The combination of calculations and experiment established the site occupied by Y ion, the main factors influencing the chemical shift, and the random nature of Sn/Ti distribution on the substituted sites.

Site occupancy disorder for hydroxyl protons is a typical occurrence in hydrous minerals. A combined experimental and GIPAW study of two hydrous magnesium silicates of the humite group showed how to use calculated ^{17}O NMR parameters to support the dynamic disorder model that involves rapid proton exchange [66].

Another case of the effect of disorder on observable properties refers to the study of ^{77}Se and ^{67}Zn chemical shifts in ZnSe nanoparticles [67]. NMR calculations on a system containing up to 17 ZnSe layers show a broad distribution of chemical shifts as a result of electronic disorder, even for the positionally ordered nanoparticle.

In some sense an extreme case of positional disorder is presented by a glass system. Double rotation NMR technique (DOR) has been applied to study ^{17}O signal in vitreous B_2O_3 [68]. The two distinct oxygen sites were resolved and identified as belonging to the boroxol ring [B_3O_6] and to non-boroxol [BO_3] groups. This assignment of experimental results became possible from comparison of the full chemical shift tensor, as well as the EFG tensor, to the calculated properties of caesium enneaborate, $Cs_2O{\cdot}9B_2O_3$, that has similar structural elements. A complementary study has been performed using ^{11}B NMR parameters for several crystal borate structures with a further extension to glassy phase [69].

It is sometimes instructive to cross the boundary between organic and inorganic systems, as was shown in an extensive study of ^{25}Mg NMR of Mg oxyanion systems [70]. Mg NMR has been used primarily for inorganic systems, although it is now shown to be a sensitive probe for studies of metal centres in biologically relevant organic molecules. CASTEP results showed good correlation with experimental values of both chemical shifts and quadrupole coupling parameters. One of the important methodological conclusions is that the use of accurate experimental structures seems to be preferred to structures optimized using CASTEP, whether optimization involves only protons or all atoms.

"NMR crystallography" methods were applied using $^{79/81}$Br and ^{25}Mg NMR shifts and quadrupolar coupling to refine the structure of $MgBr_2$; it has been shown that C_Q ($^{79/81}$Br) is extremely sensitive to the details of the structure, and the measured and calculated results for the optimized crystal structure agree within experimental error [71].

A detailed analysis of the ^{27}Al NMR parameters for 20 distinct aluminium sites in 12 crystalline oxides was presented [72]. The description of the isotropic chemical shift is very accurate, with the RMS deviation of about 2 ppm, and C_Q parameters are found typically within 1 MHz. The quality of the results allowed authors to suggest a quantitative connection between chemical shifts and Al–O bond order, and to support the conjecture by analysing the effect of pressure on calculated properties.

The issue of hydrogen bonding and its effect on NMR parameters is of fundamental interest in inorganic materials, even though perhaps its importance is not as high as in organic studies. An example investigation is that of a layered γ-titanium phosphate where calculations were used to confirm the assignment of the ^{1}H NMR spectra. An unambiguous assignment was possible, and also a proof of the hydrogen bonding between layers was provided [73].

The use of transition metal nuclei in solid-state NMR studies is relatively new, and more work is required to establish the limits of validity of GIPAW calculations for such systems. An important methodological paper showed that isotropic chemical shifts for ^{49}Ti and ^{51}V nuclei in a variety of organometallic and inorganic compounds can be successfully reproduced, while there are potential problems with reproducing the shielding tensor eigenvalues with the DFT approach [74].

GIPAW results were used to assign and interpret NMR spectra for a variety of materials: ^{13}C and ^{29}Si in two polymorphs of SiC [75]; ^{19}F in two complex fluorides, β-$BaAlF_5$ and $Ba_3Al_2F_{12}$, supported by analysis of 15 other metal fluorides [76]; $^{35/37}$Cl in Al, Ga, and In chlorides [77]; ^{27}Al in kaolinite [78]; ^{31}P and ^{27}Al in the aluminophosphate framework material AlPO-15 [79]; ^{33}S in layered transition metal disulfides [80]; ^{43}Ca in a family of Ca-containing compounds [81]; ^{29}Si in crystalline and molten forsterite [82]; ^{1}H, ^{17}O, and ^{31}P for surface and bulk structures of hydroxyapatite [83], to name but a few.

This review of the recent GIPAW calculations of NMR properties shows that results for a widely varying range of materials are reliable and can be used for quantitative analysis, such as assignment of signals to specific atomic positions or structure solution of powder samples, as well as for qualitative analysis of the effects of crystal packing, guest molecules, or hydrogen bonding. More recently it has become possible to compute NMR *J*-coupling between spins [84] in the GIPAW framework, and initial applications to organic and inorganic materials have been presented. Two bond couplings $^2J_{Si-P}$ have been accurately calculated for a silicophosphate polymorph [84]. *J*-couplings across both covalent and hydrogen bonds have been illustrated for the case of two 6-aminofulvene-1-aldimine derivatives and for the ribbon structure formed by a deoxyguanosine derivative [85], and also for glycine and uracil [86]. *J*-couplings were calculated in these studies between carbon, oxygen, and nitrogen nuclei in very good agreement with experiment, typically within 1 Hz.

There are of course some systems where both experimental and theoretical investigation of NMR properties is still in its infancy, and more work is required to establish reliable standards and interpret observed spectra. A typical example of such open area

is the ^{209}Bi study of bismuth oxyhalides where calculated C_Q parameters are underestimated and the span of chemical shift tensor components is greatly overestimated [87]. Work still remains to be done in quantifying the role of relativistic effects, and the limitations of present density functionals in such materials.

It appears that in many aspects the methodology for GIPAW studies of organic and inorganic materials is the same, although one can find notable exceptions. For example, as discussed above, various examples exist where organic materials are described more accurately when experimental structure is used rather than the DFT-optimized one. On the other hand, there is a clear example of a microporous aluminophosphate AlPO-14 where the results of ^{27}Al–^{31}Si experiments cannot be explained even qualitatively unless the structure is optimized first [88]. Certainly the input crystal structure plays a significant role in the accuracy of the computed NMR parameters, and future work must clarify the relationship between the calculation of NMR parameters, diffraction studies and the role of dynamics.

4. Vibrational spectroscopies

Modern experimental techniques include a number of probes based on the vibrational and dielectric properties of materials. Laboratory-based techniques including Raman and infrared (IR) spectroscopies are in widespread use for analysis and characterization – with a growing interest in the applications of "terahertz spectroscopy" that focuses on the spectrum in the region of 0.3–5 THz. On the other hand, the techniques of inelastic neutron scattering (INS) or inelastic X-ray scattering (IXS) are aimed mostly at the fundamental studies of vibrational properties. The primary role of theoretical methods in any of these application areas is to predict phonon frequencies and displacement patterns for phonons with wave vectors spanning the Brillouin zone, and to calculate intensities of experimentally measurable spectra such as Raman and IR.

CASTEP provides two different methods for evaluating the dynamical matrix and hence the harmonic phonon frequencies and eigenvectors. For insulators, and particularly for polar insulators, the density functional perturbation theory method, DFPT, is preferred [89]. This is the most efficient technique, and it allows the calculation of crystal response to external electric field as well as to the atomic displacements. As a result it is possible to calculate Born effective charges, dielectric constant, LO–TO splitting, IR and Raman intensities. This technique is currently implemented in CASTEP for non spin-polarized insulators and requires the use of norm-conserving pseudopotentials. In the cases where these requirements are not met the "finite displacement" technique may be used, and a supercell approach with Fourier interpolation can be introduced to calculate frequencies at general points in the Brillouin zone. However, this method does not provide information on electric field response and cannot be used to evaluate LO–TO mode splitting or to predict IR or Raman intensities.

The above-mentioned lattice dynamics methods are framed within the harmonic approximation and are therefore most applicable to the low-temperature dynamics of ordered systems. One technique for generating vibrational properties which includes a good description of anharmonicity at finite temperatures is via the Fourier transform of the velocity autocorrelation function obtained from a molecular dynamics simulation. A recent example of such approach is the study of phase-I ammonia where a combination of MD analysis and harmonic lattice dynamics was applied to the task of quantifying and assigning vibrational modes [90]. It was shown that MD frequencies of lattice modes are in better agreement with experiment; an important drawback of this technique is inability to access LO–TO mode splitting.

4.1. Raman spectroscopy

Non-resonant Raman activities are computed in CASTEP using a hybrid method combining density functional perturbation theory with the finite displacement method. The Raman activity tensor of a mode is given by the derivative of the dielectric polarizability tensor with respect to the mode amplitude. This is evaluated using a numerical central difference approximation between polarizability tensors computed using DFPT at geometries displaced from equilibrium by small positive and negative amplitudes according to the mode eigenvector. This method is similar to that of Porezag and Pedersen [91] except for the use of DFPT to compute the dielectric polarizability.

Raman intensity evaluation has been implemented in CASTEP very recently, and application examples using this functionality are still limited. One test case involves the study of the pressure-induced phase transition in a nanocrystalline tetragonal ZrO_2 [92]. Raman spectroscopy was used in the experiment to interpret the structural changes observed in X-ray diffraction as a soft-mode transformation. A CASTEP study provided a wealth of additional information including a correct symmetry assignment of Raman active vibrational modes and a quantitative measure of the Raman intensity change around the transition. Calculated Raman frequencies agree with experiment to within 10 cm^{-1}, and the Gruneisen coefficients that describe the pressure response of the modes are within 10% of the experimental estimates. Theoretical Raman intensities and their change upon compression are also in good quantitative agreement with experiment.

Calculated Raman spectra were used to interpret the results of experimental studies of hydrogen transport in $LiBH_4$ crystals [93]. Deuterium substitution was employed as a diffusion marker, and theoretical Raman spectra for partially D-exchanged molecular units were used to interpret the measured results. This comparison revealed complete scrambling of the hydrogen isotopes and thus confirmed significant hydrogen transport at temperatures below melting.

4.2. Raman spectroscopy: Small molecules

Raman activities are often calculated for molecular crystals, and the results are compared to vibrational spectra of isolated molecules in order to distil the effects of crystalline environment. It is important to be able to calculate molecular and crystalline properties in the same theoretical framework to eliminate systematic errors related to, e.g. the use of pseudopotentials. CASTEP can be used for molecular calculations by utilising the "molecule in a box" approach whereby a molecule surrounded by vacuum is placed in a large supercell. It is possible then to investigate numerically the convergence of physical properties with respect to the distance between periodic images of the molecule.

We compared CASTEP results for a number of small molecules to accurate all-electron data in order to investigate the role of pseudopotentials, of the supercell size, of the amplitude of the finite displacement which is used in the Raman activity calculation, and other computational approximations. The PBE exchange–correlation functional and norm-conserving pseudopotentials were used throughout. Table 1 shows an overall good agreement with the all-electron results from [94,95]. We found that the use of different pseudopotentials may change the equilibrium bond length by up to 0.05 Å, vibrational frequencies by about 10–20 cm^{-1}, while the Raman activities do not change by more than 10%. It appears that simulation cell volumes and vacuum gaps adequate for converged ground-state properties and vibrational frequencies are sometimes insufficient for converged Raman activities. An increase of the supercell size from 8–10 Å to 16–20 Å had a pronounced effect on Raman activities especially in the molecules with signifi-

Please cite this article in press as: V. Milman et al., J. Mol. Struct. (THEOCHEM) (2010), doi:10.1016/j.theochem.2009.12.040

Table 1
Bond length, vibrational frequency and Raman activity for small molecules. All-electron PBE results [94,95] are given in brackets.

Molecule	Bond length (Å)	Frequency (cm^{-1})	IR intensity (Debye/Å^2/amu)	Raman activity (Å^4/amu)
H_2	0.7519 (0.7498)	4318 (4323)	N/A	169 (161)
N_2	1.0811 (1.1022)	2347 (2358)	N/A	25.6 (21.4)
Cl_2	1.978 (2.020)	548 (522)	N/A	10.6 (12.6)
P_2	1.875 (1.908)	797 (703)	N/A	65.6 (61.5)
Cu_2	2.253 (2.253)	238 (261)	N/A	37.4 (39.4)
HF	0.9376 (0.9292)	4081 (4001)	N/A	40.1 (30.8)
LiF	1.622 (1.566)	934 (915)	N/A	10.2 (14.9)
LiH	1.563 (1.604)	1408 (1380)	N/A	790 (835)
Li_2	2.725 (2.731)	331 (333)	N/A	2043 (1994)
Na_2	3.030 (3.087)	159 (157)	N/A	1096 (1352)
CO_2	1.1699 (1.1711)	650 (637)	0.53 (1.01)	N/A
		1307 (1323)	N/A	28.1 (22.4)
		2335 (2341)	13.9 (12.9)	N/A
CH_4	1.097 (1.096)	1284 (1286)	0.348 (0.300)	0.1 (0.5)
		1505 (1510)	N/A	2.4 (2.6)
		2958 (2968)	N/A	237.8 (226.9)
		3079 (3081)	0.460 (0.442)	48.2 (46.0)

cant charge transfer such as HF or LiF. We attribute this sensitivity to cell size to a high degree of spatial delocalization of the DFPT electric field response orbitals, and caution that for this kind of calculation rigorous convergence testing is required.

We also investigated the accuracy of pseudopotential results for some polyatomic molecules. Table 2 compares calculated vibrational properties of benzene to the experimental and *ab initio* results from [96]. The overall qualitative agreement is satisfactory, although Raman activities of the two strong modes are overestimated in CASTEP.

The tests were further extended to more complex molecules of lower symmetry. The first example is 2-chloro-5-methylaniline (2Cl5MA, C_7H_8NCl). Experimental IR and Raman spectra have been reported recently and compared to Hartree–Fock (HF) and DFT-B3LYP results [97]. The goal of the present test is to establish the accuracy of CASTEP results relative to experiment and to such popular quantum chemistry approaches as HF and DFT-B3LYP. The results for frequencies and Raman activities are presented in Table 3. Quantum chemistry results were obtained using 6-311++G(d,p) basis set, and complex scaling rules for vibrational frequencies were applied by the authors [97].

These results show a good overall agreement between CASTEP frequencies and Raman intensities and available experimental and quantum chemical data. Furthermore, we suggest that CASTEP results can be used to improve the interpretation of experimentally observed Raman modes. For example, the lowest observed Raman active mode at 76 cm^{-1} is previously interpreted as the mode numbered 44 in Table 3 [97], while CASTEP predicts it to be the lowest mode, numbered 45. This assignment is based on the actual frequency and also on the high calculated Raman activity of this mode. We could also suggest that the Raman mode at 1595 cm^{-1} should be assigned to mode 10 and not 11, again based on the comparison of CASTEP frequencies and Raman activities with the experimental data. This assignment removes a discrepancy between the experimental IR and Raman data. We note also that the modes 30 and 31 come out in different order in HF and B3LYP calculations: it is mode 30 that has a high Raman activity, so HF results for modes 30 and 31 have the wrong order.

Table 2
Vibrational properties of benzene; experimental and MP2 results are from [96].

Mode	Frequency (cm^{-1})			Raman activity (Å^4/amu)		
	Exp	MP2	CASTEP	Exp	MP2	CASTEP
A_{1g}	993	1015	988	71	66	91
A_{1g}	3074	3240	3119	370	350	468
E_{2g}	608	610	602	4.8	14	4.9
E_{2g}	3057	3215	3093	220	210	287
E_{2g}	1601	1645	1585	28	28	26.6
E_{2g}	1178	1199	1161	9.8	9.6	12.8
E_{1g}	847	842	836	2.0	<0.01	1.2

The final example of calculated Raman intensities of a small molecule is the comparison of CASTEP results to experimental data and to MP2/6-311G** calculated properties of *near-cis* carbamoyl ketene, OCCH–$CONH_2$ [98]. We compare the two sets of calculations in Table 4. It should be noted that the MP2 results were scaled by a factor of $\sqrt{0.9}$ for three highest energy modes, and by $\sqrt{0.88}$ for other modes. Experimental data refer to the values for ketene moiety and for the amide group as measured in different compounds, and so provide at most a guide to the actual experimental frequencies [98].

The calculations for 2-chloro-5-methylaniline and for carbamoyl ketene were carried out in the 20 Å supercells at which size the Raman activities were converged to within 1–2%. An overall typical accuracy of Raman activities calculated using CASTEP for a molecular system appears to be, on the basis of comparison to accurate quantum chemistry calculations, of the order of 10–20% which should be sufficient for application studies.

4.3. Infrared spectroscopy: Molecules and molecular crystals

Infrared spectroscopy in CASTEP is based on the DFPT implementation of the response to applied electric field [89]. IR intensities are evaluated based on the Born effective charges and on the calculated Γ-point phonon frequencies. One of the first example systems for this approach was chosen to be α-quartz where a number of experimental and DFT results for lattice dynamics and dielectric properties exist. The spectrum calculated using LDA exchange–correlation is in good quantitative agreement with experiment. It appears that the accuracy is somewhat limited by the choice of exchange–correlation functional. LDA was shown to be more accurate than PBE for phonon modes of this particular system, while the reverse is true for polarizabilities [89].

Theoretical IR spectra have been used extensively in the studies of molecular and crystalline amino acids and related compounds. Complete mode assignment together with the IR spectra calculation was reported for molecules of alanine, valine, leucine and isoleucine [99]. The spectra show clear characteristic features for zwitterionic and nonzwitterionic molecules. The same amino acids were subsequently studied in the solid-state form [100], so that the IR spectra could be compared to the molecular results. The changes in high-frequency vibronic modes are a consequence of intermolecular interactions and hydrogen bonding in solid-state. This ap-

Table 3
Vibrational properties of 2-chloro-5-methylaniline. HF, B3LYP and experimental data are from [97]. Raman activities S^R are in Å^4/amu. Both unscaled (ν) and scaled (ν_s) frequencies are shown for quantum chemistry calculations. Experimental mode assignment is based either on infrared spectrum (IR) or on Raman spectrum (R).

#	HF			B3LYP			Exp		PBE (CASTEP)	
	ν	ν_s	S^R	ν	ν_s	S^R	IR	R	ν	S^R
1	3907	3536	35.0	3680	3526	41.8	3471		3614	46.3
2	3804	3442	120.9	3576	3426	171.8	3381	3355	3494	195.1
3	3357	3038	112.8	3196	3062	130.4		3060	3131	144.9
4	3328	3012	67.2	3170	3037	81.0			3109	84.3
5	3315	3000	83.4	3152	3019	93.9	3019	3021	3083	101.6
6	3245	2937	55.2	3102	2972	58.0			3055	61.1
7	3221	2915	80.0	3074	2945	96.1	2921	2919	3026	102.1
8	3169	2868	197.2	3025	2898	270.0	2860	2861	2968	351.5
9	1810	1638	21.8	1658	1630	26.4	1616	1615	1618	33.7
10	1785	1615	21.4	1635	1607	19.4			1590	21.2
11	1756	1590	11.4	1613	1586	8.1	1584	1595	1575	0.9
12	1656	1499	2.8	1525	1499	5.2	1492	1490	1500	6.7
13	1615	1461	3.2	1501	1475	3.7	1476		1466	3.5
14	1604	1451	8.8	1487	1462	9.9	1450		1448	7.2
15	1558	1410	4.6	1449	1424	3.7	1428		1425	5.2
16	1538	1392	5.6	1416	1392	16.5	1380	1379	1376	24.1
17	1429	1293	8.2	1347	1324	13.7	1314	1314	1354	10.8
18	1405	1272	11.7	1322	1399	6.8	1297	1297	1310	13.1
19	1294	1171	4.2	1290	1268	6.9	1266	1265	1275	6.0
20	1278	1156	1.2	1198	1178	3.1	1178	1177	1183	6.3
21	1258	1138	2.6	1170	1150	2.7	1145	1145	1149	3.5
22	1176	1064	10.1	1105	1086	4.8	1096		1073	10.0
23	1158	1048	0.1	1060	1042	0.1	1044	1043	1040	12.4
24	1117	1011	7.6	1046	1028	16.6			1035	7.6
25	1097	993	4.1	1023	1006	2.4			1000	0.5
26	1077	974	0.5	961	944	1.4	944	942	949	0.9
27	1023	926	3.7	946	930	0.2			942	0.2
28	959	868	0.1	858	844	0.1	856		854	0.2
29	897	812	0.7	800	786	0.3	794		791	0.5
30	814	737	0.9	746	734	23.4	735	738	744	26.8
31	794	719	26.0	731	719	0.9			726	0.1
32	680	615	0.8	629	619	1.0	630	626	633	0.6
33	663	600	2.9	598	588	1.2	585		595	0.4
34	618	560	11.0	573	564	10.8	557	564	569	9.7
35	591	535	0.7	512	503	1.7			478	3.4
36	512	463	4.5	478	470	4.3	475	475	450	0.2
37	498	451	0.5	451	443	0.4	442		412	0.7
38	401	363	8.9	373	367	8.0		373	375	5.1
39	352	318	0.4	351	345	0.3			362	3.0
40	351	318	0.6	299	294	0.7		296	303	1.4
41	307	278	0.7	294	289	0.9			292	1.4
42	262	237	0.7	246	242	0.7			249	0.5
43	236	213	0.9	216	212	0.9		219	219	0.6
44	124	112	0.2	114	112	0.2		76	122	0.4
45	20	18	0.2	33	32	0.5			60	4.7

proach was further applied to a more challenging system, dipeptide glycyl-L-alanine crystal [101]. There are 237 vibrational modes in this system; therefore analysis of the IR spectrum is rather involved. A detailed analysis of various vibrational modes and their contribution to IR absorption represents perhaps the most challenging example of a DFPT study on a molecular crystal. A similar study was undertaken on glycine and L-alanine where the vibrational spectra computed at the optimized geometries provided a good fit to the observed IR and Raman spectra in the solid-state [102].

CASTEP IR spectroscopy was successfully applied to two examples of conjugate polymers, polyaniline, and poly(*p*-pyridil vinyline) [103]. The structural differences between the two polymers were shown to be responsible for characteristic differences in the IR absorption spectra.

Terahertz spectroscopy measures low energy excitations with frequencies below 100–150 cm^{-1}, and presents a challenging application area for computational spectroscopy. A combination of low-temperature THz spectroscopy with DFPT calculations was used to predict and explain the terahertz spectra of three different hydrogen-bonded molecular crystals: the pharmaceutical product benzoic acid, the DNA base thymine, and the saccharide sucrose [104]. The calculations showed that distinct vibrational modes found in solid-state materials are best described as phonon modes with strong coupling to the intramolecular degrees of freedom. Hence a computational method taking the periodicity of the crystal lattice as well as intramolecular motion into account is a prerequisite for the correct prediction of vibrational modes in such materials.

A complex low symmetry system 8-(*n*-butylaminophenylmethyliden)-1,2,3,4,5,6,7-heptathiocan, the product of the Asinger reaction between elemental sulfur, *n*-butylamine and acetophenone, has been studied using a variety of experimental and computational techniques [105]. CASTEP calculations on isolated molecules and on the complete unit cell were used to assign the observed vibrational bands and to analyse the effect of intermolecular interactions on the IR spectrum. It is clear from the calculations that the IR spectrum of an isolated molecule gives a very poor description of the experimental results while the solid-state calculation is sufficiently accurate for the purpose of mode assignment and analysis.

CASTEP IR spectroscopy offers useful tools in chemistry of metal hydride complexes as witnessed by, for example, a combined

Table 4
Vibrational properties of *near-cis* carbamoyl ketene. MP2 results and estimates of experimental frequencies are from [98]. PBE are present CASTEP results.

Frequency (cm^{-1})			Raman activity ($Å^4$/amu)	
MP2	PBE	Exp	MP2	PBE
3522	3637	3400	53.6	60.4
3398	3500	3244	121.2	184.3
3065	3147		69.2	71.9
2123	2258	2160	9.4	21.6
1693	1743	1690	14.1	15.6
1551	1561	1600	6.1	3.7
1379	1397	1376	24.2	19.6
1223	1238		4.9	3.4
1068	1106	1140	7.9	9.7
1045	1034	1051	19.3	15.6
879	870		4.5	3.2
713	773		0.8	0.1
650	688	587	6.9	13.8
545	603	558	0.9	2.3
524	549	510	4.9	0.3
473	505		0.5	6.2
468	432		2.1	0.2
382	403		1.3	0.9
373	193		1.5	0.1
132	138		1.9	1.7
86	103		0.4	0.2

experimental and theoretical characterization of the $[ReH_9]^{2-}$ ion [106]. This study showed that a fully periodic simulation of the barium salt $Ba[ReH_9]$ reproduces experimental IR spectrum very well, especially the internal modes of the hydride molecular ion. A calculation on an isolated ion, on the other hand, presents a spectrum with a large upshift of all frequencies relative to the barium salt case. This paper contains an instructive analysis of the pitfalls of a periodic calculation on a charged system and explains in detail the technique for obtaining properties of an isolated charged molecule by extrapolation of the results of supercell calculations.

An investigation of Raman and IR modes under compression can be a useful guide in determining stability and properties of energetic compounds used in high-performance explosives and propellant materials. Needless to say, theoretical studies of energetic materials often constitute the only source of information on the behaviour and properties under extreme conditions. One of the best studied energetic materials is a molecular crystal octahydro-1,3,5,7-tetranitro-1,3,5,7-tetrazocine (HMX). The most stable form, β-HMX, has been studied up to 40 GPa [107] and later up to 100 GPa [108] in order to quantify the pressure effect on intra- and intermolecular modes. Another material of this class is silver azide (AgN_3), a sensitive primary explosive. Vibrational mode assignment and pressure dependence of the frequencies up to 500 GPa were reported and the results related to the changes in the crystal structure and electronic properties of the material [109]. Vibrational and thermodynamic properties of three members of the nitro phenols family of compounds, crystalline 2,4-dinitrophenol, 2,4-dinitroresorcinol, and 4,6-dinitroresorcinol, were studied [110]. The calculated thermodynamic properties show that the decomposition reactions of the three solids are thermodynamically favourable at high temperature; moreover, 2,4-dinitrophenol has higher possibility to decompose than 2,4- and 4,6-dinitroresorcinol.

While Raman and IR spectroscopies dominate as the experimental methods of choice for the studies of isolated molecules and molecular crystals, INS has been making significant inroads as a useful alternative for investigations of bio-molecular systems. An example of a combined INS experimental study and a theoretical investigation is the study of indole and its derivatives where the full set of vibrational frequencies has been measured and then assigned using CASTEP results [111].

4.4. Infrared spectroscopy: Inorganic crystals

IR spectroscopy of inorganic crystals provides key information on polymorph types, local environment, and even degree of the long-range order. A good example is a study of the effect of crystalline order on the IR spectrum of calcite [112]. The agreement between calculated LDA phonon frequencies for ideal calcite and experiment is never worse than 30 cm^{-1} and is usually substantially better. IR spectra were calculated for strained configurations of crystalline calcite to model the local strains in amorphous calcite. An analysis of the correlation between calculated spectra for distorted structures and the experimental results for a mixture of amorphous and crystalline calcite yields semi quantitative agreement, even for simplified representation of disorder.

CASTEP IR reflectance spectra have been reported for three BN modifications (cubic, wurtzite and hexagonal) and found to be in excellent agreement with experiment [113]. Phonon frequencies, including LO–TO splitting, and dielectric constants match experimental data well, so the good agreement for the spectra themselves was to be expected.

Dielectric properties as well as IR and Raman frequencies have been used to analyse the differences between two complex perovskites, ordered $Ba(Mg_{1/3}Ta_{2/3})O_3$ (BMT) and $Ba(Mg_{1/3}Nb_{2/3})O_3$ (BMN) [114]. These are representative materials for the class of new microwave dielectric ceramics, and CASTEP calculations provided the first assignment of their far-IR absorption peaks. A comparison of the two materials showed that the larger polarizability of Ta ion explains the difference in oxygen oscillation amplitude, and hence the smaller permittivity of BMT. A similar study was also performed for a different member of this group of materials, $Ba(Zn_{1/3}Nb_{2/3})O_3$ (BZN), where the dipole interaction was found to be responsible for the variation in dielectric properties [115]. Vibrational properties of the ordered BMT material were independently calculated and subsequently used to interpret the experimental spectra of the disordered phase [116].

First principles studies were applied to investigate properties of promising high-temperature thermoelectric materials, types I and II silicon clathrates [117]. Calculated IR spectra were analysed to explain the differences in vibrational spectra of type I (simple cubic lattice, 46 atoms per unit cell) and type II (face centred cubic lattice, 136 atoms per cubic cell) clathrates.

IR and Raman intensities as calculated by CASTEP are of course vital for the actual spectra calculation. However, as a first step in the analysis of vibrational properties, it might be sufficient to calculate and assign frequencies of IR and Raman active vibrational modes. Examples include a systematic study of the Γ-point modes in a nonlinear optical material CsB_3O_5 [118], a microwave dielectric material $MgTiO_3$ [119,120], negative thermal expansion materials $Cd(CN)_2$ and $Zn(CN)_2$ [121]. Similarly one can employ CASTEP calculations to investigate a vibrational signature of defects by, e.g. predicting local vibrational modes for a number of possible defects in different charge states as was done for BH and BH_2 centres in diamond [122].

4.5. Phonon dispersion

Optical electromagnetic radiation couples only long wavelength vibrational modes, which means that IR and Raman spectroscopy can measure only phonon frequencies at zero wavevector, the Γ-point. But the selection rules of inelastic neutron spectroscopy (INS) and more recently inelastic X-ray spectroscopy (IXS) are not so restricted, allowing coupling to phonons at a range of wavevectors spanning the Brillouin Zone. Consequently these techniques are used to measure phonon dispersion curves and vibrational densities of states (VDOS) of solids over a full range of wavevectors. This allows the study of lattice dynamical contribu-

tion to a broader range of structural and thermodynamic phenomena than is feasible with IR and Raman spectroscopy. For example, the ability to measure dispersion curves permits the study of soft modes at the BZ boundary associated with phase transitions involving a doubling of the unit cell. And a vibrational density of states integrated across the Brillouin Zone may be used to compute thermodynamic properties including vibrational free energy and entropy, specific heat capacity, Debye temperature and the like. *Ab initio* lattice dynamics calculations using DFPT or finite-displacement/supercell methods are very well adapted to complement such experiments. The quality of the match between DFT calculation and INS experiment is well illustrated in a range of materials such as α-quartz and the ionic molecular crystal $NaHF_2$ [89].

An example of a soft-mode behaviour study is the investigation of the softening of the TA mode at the Brillouin zone boundary point X in rock-salt alkali hydrides (LiH, NaH, KH, RbH, and CsH) [123]. The structural instability which is manifested by the decrease of the TA(X) frequency under compression and by the related softening of the C_{44} elastic coefficient was used as an explanation of the pressure-induced transition from the NaCl to CsCl structure. The same mechanism was identified in the high-pressure behaviour of CaO [124].

Phonon dispersion and density of states for two types of Si clathrate materials and for Si crystals were calculated and used to evaluate thermodynamic properties of these thermoelectric materials [117]. The lattice heat capacity, lattice thermal conductivity and the Seebeck coefficient were found to be in good agreement with the scarce experimental data available. Another example of the phonon dispersion, DOS and thermodynamical properties calculation is presented in the study of Mg_2Si and Mg_2Ge, also potential thermoelectric materials [125]. The Γ-point frequencies agree with experiment to within 5 cm^{-1}, and the deviations from experiment for calculated entropy, heat capacity and Debye temperature are extremely small: 1.4%, −0.4%, and 3.6%, respectively.

The B–C–N system currently attracts much interest as a source of new ceramic materials with good mechanical and thermal properties. Lattice dynamical studies using CASTEP were performed for β-BC_2N in comparison to the related materials, cubic BN and diamond [126]. An analysis of phonon dispersion, DOS, heat capacity and Debye temperature provided an explanation for higher heat capacity of BN and BC_2N compounds relative to diamond.

First principles calculations of phonon frequencies can be used to guide and interpret lattice dynamics experiments as was shown recently in an IXS study [127,128]. Predictive lattice dynamics was used to guide the experimental procedure by computing in advance the locations of modes in (q, ω) space. This allowed scattering geometries to be chosen to optimize the experiment and avoid waste of beam time searching for the modes of interest. *Ab initio* calculations simplify IXS measurements, as the computed dynamical matrix can be used to calculate the dynamical structure factor for a variety of wave vector transfers so that optimal scattering geometries can be chosen in advance. This approach was used to discover a large, unexpected dispersion of the OH-stretching frequencies in diaspore [127] – the first ever measurement of dispersion of OH stretch modes in a solid. A subsequent development of the technique allowed to combine CASTEP calculations with powder IXS to reconstruct the full lattice dynamics of stishovite [128]. This is an important methodological achievement since typical inelastic scattering experiments, neutron or X-ray, are performed on large single crystals which significantly reduces the range of applicability of these techniques. The results of the combined experimental and theoretical study were used to calculate thermodynamic properties, including heat capacity, entropy, Debye temperature, in excellent agreement with experiment. The calculations involved in this study are demanding as phonon frequencies are required on a rather fine mesh in the Brillouin zone ($30 \times 30 \times 50$ grid was used in [128]) but the associated benefits of an accurate calculation of material properties are obvious.

A novel way of combining theoretical lattice dynamics with yet another experimental technique, thermal diffuse scattering of X-rays (TDS), was presented [129]. Phonon frequencies and eigenvectors of Zn were obtained using the finite displacement method with a $4 \times 4 \times 3$ supercell. This information was used to interpret non-monotonic intensity variations in the thermal diffuse scattering which correspond to the occurrence of a Kohn anomaly in the phonon dispersion. It was then possible to associate the 3D objects in TDS results with pieces of the Fermi surface providing a unique tool for Fermi surface visualization.

5. Optical spectroscopy

One important aspect of the optical spectroscopy, namely infrared and far infrared spectra, has been discussed already in the context of lattice contributions to the dielectric function, $\varepsilon(\omega)$. Another important area for spectroscopy is visible and UV range of photon energies (up to 10–20 eV) where the dielectric loss is determined by electronic transitions rather than by the phonon contributions. CASTEP calculates optical properties by applying the Fermi's golden rule expression. This calculation requires an evaluation of the matrix element in the dipole approximation, of the eigenvalues of the valence and conduction bands, and then a Kramers–Kronig transformation of the obtained imaginary part of the dielectric function. The method has obvious limitations, neglect of local field effects and many-body effects and underestimation of the DFT band gap being the most important ones. The examples below nevertheless demonstrate that CASTEP results provide useful qualitative and quantitative information on optical properties of materials.

5.1. Linear optical properties

We review here a few investigations where such properties as dielectric function, refractive index, absorption, and reflection coefficient were calculated as part of a material characterization. The typical goals of such calculations are either to predict optical spectra of new materials or of known materials but under extreme conditions, or to achieve better understanding of properties of existing materials in connection to their electronic structure. These calculations are sufficiently routine now, so we will look below only at the most recent examples with significant application promise.

The first set of examples includes new or highly relevant materials where one can get an estimate of the DFT accuracy. For example, the dielectric function, absorption spectrum, refractive index, extinction coefficient, reflectivity, and energy loss coefficient of cubic and tetragonal $BaTiO_3$ were calculated and found to be in good agreement with experimental data in a wide energy range [130]. The dielectric function of a newly synthesized gadolinium molybdate $Na_5Gd(MoO_4)_4$ was calculated [131]. The static refractive index of 2.06 is very close to the generally accepted value of 2.0 for other molybdate crystals.

Linear optical properties of lithium thiogallate, $LiGaS_2$, were measured and calculated in the IR to visible part of the spectrum [132]. A comparison of the calculated electronic structure with the experimental XPS data suggested that the use of DFT + U method [26] was essential for a correct description of Ga 3d-states. Absorption coefficient and refractive index calculated in this approach show very good agreement with experiment and lay a foundation for the study of nonlinear optical properties of this material. Glycine–sodium nitrate is a typical member of the group of semi-

organic materials that are being suggested for nonlinear optical applications. The dielectric function of this material was predicted and analysed in detail [133], followed by the experimental study which confirmed good quantitative agreement for the adsorption spectrum [134].

Adsorption spectra of α-glycine crystals were measured and calculated in an attempt to fill the gap in the information on optical properties of crystalline amino acids. The calculated optical absorption is highly dependent on the polarization of the incident radiation due to the spatial arrangement of the dipolar glycine molecules; in the case of a polycrystalline sample, the first-principles calculated optical absorption is in good agreement with the measurement when a rigid energy shift is applied [135].

The level of accuracy presented by such studies, given the known sources of errors listed above, inspires numerous predictive studies. A representative selection of recent results is given below.

The effect of In doping of SnO_2 on optical properties of this typical transparent conducting oxide has been studied in [136]. It was shown that the main changes due to increased In concentration are in the IR region rather than in the visible or UV part of the spectrum. A systematic study of optical properties of $Zn_xCd_{1-x}Te$ mixed crystals has been reported [137]. A nontrivial dependence on Zn concentration in this important optoelectronic material was found and related to the changes in the calculated band structure. Another set of potentially useful optoelectronic materials includes AlN polymorphs. 2*H*-AlN polymorph is already finding commercial applications, and the DFT study showed that other polymorphs such as 4*H*- and 6*H*-AlN have similar optical properties and hence have the same application potential [138].

Calculated optical properties of a new promising dielectric material, V_4AlC_3, suggest that this material, due to the combination of mechanical and optical properties, has a potential for spacecraft coating to avoid solar heating [139]. The spectra of triclinic $CdSiO_3$, a typical host material for long lasting phosphorescence applications, were calculated and analyzed in detail, especially in relation to the predicted anisotropy and its connection to the polyhedra alignment in the structure [140].

A calculation of optical absorption of Al_2O_3 and $MgSiO_3$ under compression up to 220 GPa was used in order to explain experimentally observed loss of the optical transparency of alumina, and to suggest an explanation for an increase in electrical conductivity in $MgSiO_3$ in the Earth's lower mantle. The main conclusion is that, despite the band gap decrease and the structural phase transition, the suggested explanation for the change in optical properties is the increased role of defects, in particular +2 charge oxygen vacancies [141].

5.2. Nonlinear optical properties

The development of highly efficient nonlinear optical (NLO) crystals is of great importance to extend the frequency range provided by conventional laser sources into the ultraviolet and infrared regions. Therefore, the search for new NLO crystals is still very active. There is a number of sometimes conflicting requirements to good NLO materials: large second harmonic generation (SHG) coefficients, a wide transparent and phase matchable region, good optical quality, and a high damage threshold. A computational screening of possible NLO materials has a potential for generating good candidate crystals, and a study of known NLO systems is useful in understanding the fundamental reasons for their good performance.

The prerequisites for a search for an NLO material is the ability to calculate both linear (refractive index, n) and nonlinear (SHG) optical properties that are related to second order susceptibility $\chi^{(2)}$. The formalism for calculating the static limit of $\chi^{(2)}$ using CASTEP methodology has been described and applied as early as 1999 [142]. This paper also introduced a "real-space atom-cutting" methodology that allows to identify the parts of the structure that are mostly responsible for the nonlinear optical properties; this technique was further extended by adding a band-resolved analysis [143]. The studies of NLO materials by necessity include calculation of linear optical properties as well, thus can be considered as an additional example of the work described in the previous section.

The first NLO material studied using CASTEP was β-BaB_2O_4 [142]. Refractive index in the relevant energy range was shown to agree with experiment to within 0.1, while the birefringence, $\Delta n = |n_o - n_s|$, was accurate to about 0.001. SHG coefficients d_{ij} reproduced correct orientational dependence, and were in good quantitative agreement with experiment. The method has been applied subsequently to a variety of NLO materials. Some studies aimed at validation of the method by comparing the results with experimental data, and at elucidation of the role played by specific anion group. Borates, a very popular group of inorganic NLO crystals, have been studied in great detail with the results reported for LiB_3O_5, CsB_3O_5, and $CsLiB_6O_{10}$ (n within 0.05 of experiment, Δn within 0.005, d_{ij} within 0.1–0.5) [144], BiB_3O_6 (d_{ij} within about 0.5) [145], $Sr_2Be_2B_2O_7$, $Ba_2Al_2B_2O_7$ and $K_2Al_2B_2O_7$ (n and Δn within 0.01 of experiment, d_{ij} within 0.1) [146], $KBe_2BO_3F_2$ (n and Δn within 0.01 of experiment, d_{ij} within 0.1–0.2) [147]. Another promising family of materials under investigation is tetragonal ternary chalcopyrites, e.g. $AgGaX_2$ (X = S, Se, Te) (n within 0.1 of experiment, Δn within 0.01, d_{ij} within 20%) [148] or $LiGaX_2$ (X = S, Se, Te) [149,150], and solid solutions of the composition $AgGa(S_xSe_{1-x})_2$ where CASTEP calculations correctly predict the effect of concentration on the SHG coefficient values [151].

Molecular NLO crystals such as KDP (KH_2PO_4) and urea are among the first materials experimentally suggested for SHG applications; CASTEP results explain experimental properties very accurately for these materials (n within 0.05 of experiment, Δn within 0.01, d_{ij} within 0.1) [152].

The same technique has been applied to study molecules in the supercell geometry. The property of interest in this case is the first-order hyperpolarizability, β. The study of para-, meta- and ortho-push–pull benzene (nitroaniline) and of push–pull polyenes showed that the order of magnitude of β is reproduced well; importantly, all the qualitative trends such as the effect of configuration and of the length of a polyene chain are reproduced in CASTEP calculations [143].

Predictive studies have been presented aimed at discovery of new NLO materials such as orthorhombic ternary nitrides [153] or $CsGeBr_3$ [154]. The computational approach allowed also excluding certain candidate materials such as crystals with only a Be–O anionic group. They may have promising SHG values as in the case of $SrBe_3O_4$ [155], but the birefringence of this family of compounds was predicted to be too low [156]. A similarly negative conclusion was reached for fluorides Na_2SbF_5, $BaMgF_4$, and $BaZnF_4$ that appear to possess too low SHG values [157].

An approximate way of accessing NLO properties is via an anharmonic oscillator (AHO) model [158,159]. This model expresses the second order susceptibilities as a product of three first-order susceptibilities that are straightforwardly obtained from the dielectric function. This approach was applied to diamond and four polymorphs of C_3N_4 [158] and to the new promising material $BaNbIO(IO_3)_5$ [159]. The results are in qualitative agreement with experiment; an advantage of the AHO model over the direct calculation of the second order susceptibilities is the ease of obtaining the dispersion of SHG coefficients. While the atom-cutting and band-resolved techniques of the direct calculation scheme do offer better understanding of the role of various structural units, the results are mostly reported in a static limit, while it's important for applications to evaluate SHG at a given laser wavelength.

Please cite this article in press as: V. Milman et al., J. Mol. Struct. (THEOCHEM) (2010), doi:10.1016/j.theochem.2009.12.040

6. Conclusions

We presented a review of the main areas of CASTEP applications in the general field of spectroscopy, including in particular solid-state NMR spectroscopy, electron energy loss spectroscopy, IR and Raman vibrational spectroscopy, linear and nonlinear optical spectroscopy. In addition to the analysis of the published data we present the results of novel EELS calculations for two niobium oxides that confirm the likely role of EELS as an analytical tool for phase analysis of a mixture of niobium oxides. We also report vibrational properties including Raman and IR intensities for a group of small and medium sized molecules in comparison with all-electron calculations to illustrate the level of achievable accuracy in pseudopotential calculations.

Analysis of the results surveyed here allows us to conclude that CASTEP provides a reliable set of analytical tools that can be used in conjunction with experimental spectroscopic studies to verify, explain and predict spectral properties of a wide range of materials.

References

[1] N. Marzari, MRS Bull. 31 (2006) 681–687.
[2] A.R. Oganov, Z. Kristallogr. 220 (2005) V.
[3] B. Winkler, Introduction to high pressure computational crystallography, in: A. Katrusiak, P. McMillan (Eds.), NATO Advanced Research Workshop on High-Pressure Crystallography, Springer, Erice, Italy, 2003, pp. 159–177.
[4] C.J. Pickard, R.J. Needs, J. Phys.: Condens. Matter 21 (2009) 452205.
[5] European Theoretical Spectroscopy Facility. Available from: <http://www.etsf.eu/>.
[6] S.J. Clark, M.D. Segall, C.J. Pickard, P.J. Hasnip, M.I.J. Probert, K. Refson, M.C. Payne, Z. Kristallogr. 220 (2005) 567–570.
[7] Accelrys 2008, Materials Studio 4.4.
[8] L. Kleinman, D.M. Bylander, Phys. Rev. Lett. 48 (1982) 1425–1428.
[9] D. Vanderbilt, Phys. Rev. B 41 (1990) 7892–7895.
[10] M.C. Payne, M.P. Teter, D.C. Allan, T.A. Arias, J.D. Joannopoulos, Rev. Mod. Phys. 64 (1992) 1045–1097.
[11] G. Kresse, J. Furthmüller, Phys. Rev. B 54 (1996) 11169–11186.
[12] D. Alfè, Comput. Phys. Commun. 118 (1999) 31–33.
[13] N. Marzari, D. Vanderbilt, M.C. Payne, Phys. Rev. Lett. 79 (1997) 1337–1340.
[14] C.J. Pickard, M.C. Payne, Electron Microsc. Anal. 153 (1997) 179–182.
[15] C.J. Pickard, Ph.D. Thesis, University of Cambridge, 1997.
[16] P. Rez, J.R. Alvarez, C. Pickard, Ultramicroscopy 78 (1999) 175–183.
[17] D.N. Jayawardane, C.J. Pickard, L.M. Brown, M.C. Payne, Phys. Rev. B 64 (2001) 115107.
[18] S.P. Gao, C.J. Pickard, M.C. Payne, J. Zhu, J. Yuan, Phys. Rev. B 77 (2008) 115122.
[19] S.-P. Gao, A. Zhang, J. Zhu, J. Yuan, Appl. Phys. Lett. 84 (2004) 2784–2786.
[20] S.-P. Gao, J. Zhu, J. Yuan, Chem. Phys. Lett. 400 (2004) 413–418.
[21] S.-P. Gao, J. Jiang, M. Cao, J. Zhu, J. Yuan, Phys. Rev. B 69 (2004) 214419.
[22] C. Hébert, Micron 38 (2007) 12–28.
[23] S.-P. Gao, C.J. Pickard, A. Perlov, V. Milman, J. Phys.: Condes. Matter 21 (2009) 104203.
[24] G. Gregori, H.-J. Kleebe, H. Mayr, G. Ziegler, J. Eur. Ceram. Soc. 26 (2006) 1473–1479.
[25] J.A. Aguiar, M. Asta, N. Grönbech-Jensen, A. Perlov, V. Milman, S. Gao, C. Pickard, N.D. Browning, J. Phys.: Conf. Ser., in press.
[26] V.I. Anisimov, J. Zaanen, O.K. Andersen, Phys. Rev. B 44 (1991) 943–954.
[27] C.R. Seabourne, A.J. Scott, R. Brydson, EELS modelling using a pseudopotential DFT code, in: EMC 2008 14th European Microscopy Congress 1–5 September 2008, Aachen, Germany, 2008, pp. 437–438.
[28] C.R. Seabourne, A.J. Scott, R. Brydson, R.J. Nicholls, Ultramicroscopy 109 (2009) 1374–1388.
[29] S. Lozano-Perez, V.D. Bernal, R.J. Nicholls, Ultramicroscopy 109 (2009) 1217–1228.
[30] D. Bach, H. Stormer, R. Schneider, D. Gerthsen, J. Verbeeck, Microsc. Microanal. 12 (2006) 416–423.
[31] M.J. Olszta, J. Wang, E.C. Dickey, J. Microsc. 224 (2006) 233–241.
[32] R.W.G. Wyckoff, Defective rocksalt structure, in: Crystal Structures, Interscience Publishers, New York, 1963, pp. 85–237.
[33] O. Madelung, U. Rössler, M. Schulz, Nb_2O_5: crystal structure, lattice parameters of M-Nb_2O_5, in: Non-Tetrahedrally Bonded Binary Compounds II, Springer-Verlag, 2000, pp. 1–4.
[34] J.P. Perdew, K. Burke, M. Ernzerhof, Phys. Rev. Lett. 77 (1996) 3865–3868.
[35] Available from: <http://www.webelements.com>.
[36] C.P. Grey, R. Tycko, Phys. Today 62 (2009) 44–49.
[37] C.J. Pickard, F. Mauri, Phys. Rev. B 63 (2001) 245101.
[38] J.R. Yates, C.J. Pickard, F. Mauri, Phys. Rev. B 76 (2007) 024401.
[39] C.J. Pickard, F. Mauri, Phys. Rev. Lett. 88 (2002) 086403.
[40] F. Mauri, N. Vast, C.J. Pickard, Phys. Rev. Lett. 87 (2001) 085506.
[41] M. Profeta, F. Mauri, C.J. Pickard, J. Am. Chem. Soc. 125 (2002) 541–548.
[42] R.K. Harris, P. Hodgkinson, C.J. Pickard, J.R. Yates, V. Zorin, Magn. Reson. Chem. 45 (2007) S174–S186.
[43] J.C. Johnston, R.J. Iuliucci, J.C. Facelli, G. Fitzgerald, K.T. Mueller, J. Chem. Phys. 131 (2009) 144503.
[44] J.F. Zhu, A.J. Geris, G. Wu, Phys. Chem. Chem. Phys. 11 (2009) 6972–6980.
[45] J.R. Yates, T.N. Pham, C.J. Pickard, F. Mauri, A.M. Amado, A.M. Gil, S.P. Brown, J. Am. Chem. Soc. 127 (2005) 10216–10220.
[46] A.C. Uldry, J.M. Griffin, J.R. Yates, M. Perez-Torralba, M.D.S. Maria, A.L. Webber, M.L.L. Beaumont, A. Samoson, R.M. Claramunt, C.J. Pickard, S.P. Brown, J. Am. Chem. Soc. 130 (2008) 945–954.
[47] A. Zheng, S.B. Liu, F. Deng, J. Comput. Chem. 30 (2009) 222–235.
[48] J.N. Latosinska, Chem. Phys. Lett. 463 (2008) 195–200.
[49] J.P. Bradley, C. Tripon, C. Filip, S.P. Brown, Phys. Chem. Chem. Phys. 11 (2009) 6941–6952.
[50] L.A. O'Dell, R.W. Schurko, Phys. Chem. Chem. Phys. 11 (2009) 7069–7077.
[51] J.S. Filhol, J. Deschamps, S.G. Dutremez, B. Boury, T. Barisien, L. Legrand, M. Schott, J. Am. Chem. Soc. 131 (2009) 6976–6988.
[52] E. Salager, R.S. Stein, C.J. Pickard, B. Elena, L. Emsley, Phys. Chem. Chem. Phys. 11 (2009) 2610–2621.
[53] L. Seyfarth, J. Sehnert, N.E.A. El-Gamel, W. Milius, E. Kroke, J. Breu, J. Senker, J. Mol. Struct. 889 (2008) 217–228.
[54] H.A. Fruchtl, T. van Mourik, C.L. Pickard, J.D. Woollins, Chem. Eur. J. 15 (2009) 2687–2692.
[55] R.K. Harris, P. Hodgkinson, T. Larsson, A. Muruganantham, I. Ymen, D.S. Yufit, V. Zorin, Cryst. Growth Des. 8 (2008) 80–90.
[56] J.J. Harrison, C.Y. Chan, A. Onopchenko, A.R. Pradhan, M. Petersen, Magn. Reson. Chem. 46 (2008) 115–124.
[57] J.N. Dumez, C.J. Pickard, J. Chem. Phys. 130 (2009) 104701.
[58] S. Cadars, A. Lesage, C.J. Pickard, P. Sautet, L. Emsley, J. Phys. Chem. A 113 (2009) 902–911.
[59] E. Zurek, C.J. Pickard, J. Autschbach, J. Am. Chem. Soc. 129 (2007) 4430–4439.
[60] E. Zurek, C.J. Pickard, J. Autschbach, J. Phys. Chem. C 112 (2008) 9267–9271.
[61] E. Zurek, C.J. Pickard, J. Autschbach, J. Phys. Chem. C 112 (2008) 11744–11750.
[62] E. Zurek, C.J. Pickard, J. Autschbach, J. Phys. Chem. A 113 (2009) 4117–4124.
[63] E. Zurek, C.J. Pickard, B. Walczak, J. Autschbach, J. Phys. Chem. A 110 (2006) 11995–12004.
[64] L. Lai, J. Lu, W. Song, M. Ni, L. Wang, G.F. Luo, J. Zhou, W.N. Mei, Z.X. Gao, D.P. Yu, J. Phys. Chem. C 112 (2008) 16417–16421.
[65] S.W. Reader, M.R. Mitchell, K.E. Johnston, C.J. Pickard, K.R. Whittle, S.E. Ashbrook, J. Phys. Chem. C 113 (2009) 18874–18883.
[66] J.M. Griffin, S. Wimperis, A.J. Berry, C.J. Pickard, S.E. Ashbrook, J. Phys. Chem. C 113 (2009) 465–471.
[67] S. Cadars, B.J. Smith, J.D. Epping, S. Acharya, N. Belman, Y. Golan, B.F. Chmelka, Phys. Rev. Lett. 103 (2009) 136802.
[68] A. Wong, A.P. Howes, B. Parkinson, T. Anupold, A. Samoson, D. Holland, R. Dupree, Phys. Chem. Chem. Phys. 11 (2009) 7061–7068.
[69] S. Sen, Mol. Simul. 34 (2008) 1115–1120.
[70] L.S. Cahill, J.V. Hanna, A. Wong, J.C.C. Freitas, J.R. Yates, R.K. Harris, M.E. Smith, Chem. Eur. J. 15 (2009) 9785–9798.
[71] C.M. Widdifield, D.L. Bryce, Phys. Chem. Chem. Phys. 11 (2009) 7120–7122.
[72] M. Choi, K. Matsunaga, F. Oba, I. Tanakat, J. Phys. Chem. C 113 (2009) 3869–3873.
[73] L. Mafra, J. Rocha, C. Fernandez, G.R. Castro, S. Garcia-Granda, A. Espina, S.A. Khainakov, J.R. Garcia, Chem. Mater. 20 (2008) 3944–3953.
[74] L. Truflandier, M. Paris, F. Boucher, Phys. Rev. B 76 (2007) 035102.
[75] J.S. Hartman, B. Berno, P. Hazendonk, C.W. Kirby, E. Ye, J. Zwanziger, A.D. Bain, J. Phys. Chem. C 113 (2009) 15024–15036.
[76] A.M. Zheng, S.B. Liu, F. Deng, J. Phys. Chem. C 113 (2009) 15018–15023.
[77] R.P. Chapman, D.L. Bryce, Phys. Chem. Chem. Phys. 11 (2009) 6987–6998.
[78] B. Zhou, B.L. Sherriff, T. Wang, Am. Miner. 94 (2009) 865–871.
[79] P.J. Byrne, J.E. Warren, R.E. Morris, S.E. Ashbrook, Solid State Sci. 11 (2009) 1001–1006.
[80] A. Sutrisno, V.V. Terskikh, Y. Huang, Chem. Commun. (2009) 186–188.
[81] D.L. Bryce, E.B. Bultz, D. Aebi, J. Am. Chem. Soc. 130 (2008) 9282–9292.
[82] S. Sen, J. Tangeman, Am. Miner. 93 (2008) 946–949.
[83] H. Chappell, M. Duer, N. Groom, C. Pickard, P. Bristowe, Phys. Chem. Chem. Phys. 10 (2008) 600–606.
[84] S.A. Joyce, J.R. Yates, C.J. Pickard, F. Mauri, J. Chem. Phys. 127 (2007) 204107.
[85] S.A. Joyce, J.R. Yates, C.J. Pickard, S.P. Brown, J. Am. Chem. Soc. 130 (2008) 12663–12670.
[86] I. Hung, A.C. Uldry, J. Becker-Baldus, A.L. Webber, A. Wong, M.E. Smith, S.A. Joyce, J.R. Yates, C.J. Pickard, R. Dupree, S.P. Brown, J. Am. Chem. Soc. 131 (2009) 1820–1834.
[87] H. Hamaed, M.W. Laschuk, V.V. Terskikh, R.W. Schurko, J. Am. Chem. Soc. 131 (2009) 8271–8279.
[88] S.E. Ashbrook, M. Cutajar, C.J. Pickard, R.I. Walton, S. Wimperis, Phys. Chem. Chem. Phys. 10 (2008) 5754–5764.
[89] K. Refson, P.R. Tulip, S.J. Clark, Phys. Rev. B 73 (2006) 155114.
[90] A.M. Reilly, D.S. Middlemiss, M.M. Siddick, D.A. Wann, G.J. Ackland, C.C. Wilson, D.W.H. Rankin, C.A. Morrison, J. Phys. Chem. A 112 (2008) 1322–1329.
[91] D. Porezag, M.R. Pederson, Phys. Rev. B 54 (1996) 7830–7836.
[92] V. Milman, A. Perlov, K. Refson, S.J. Clark, J. Gavartin, B. Winkler, J. Phys.: Condes. Matter 21 (2009) 485404.

Please cite this article in press as: V. Milman et al., J. Mol. Struct. (THEOCHEM) (2010), doi:10.1016/j.theochem.2009.12.040

[93] R. Gremaud, Z. Lodziana, P. Hug, B. Willenberg, A.M. Racu, J. Schoenes, A.J. Ramirez-Cuesta, S.J. Clark, K. Refson, A. Zuttel, A. Borgschulte, Phys. Rev. B 80 (2009) 100301.
[94] D.C. Patton, D.V. Porezag, M.R. Pederson, Phys. Rev. B 55 (1997) 7454–7459.
[95] D.C. Patton, D.V. Porezag, M.R. Pederson, Phys. Rev. B 57 (1998) 1995.
[96] P.E. Maslen, N.C. Handy, R.D. Amos, D. Jayatilaka, J. Chem. Phys. 97 (1992) 4233–4254.
[97] M. Karabacak, D. Karagöz, M. Kurt, J. Mol. Struct. 892 (2008) 25–31.
[98] H.M. Badawi, J. Mol. Struct. 888 (2008) 379–385.
[99] P.R. Tulip, S.J. Clark, J. Chem. Phys. 121 (2004) 5201–5210.
[100] P.R. Tulip, S.J. Clark, Phys. Rev. B 74 (2006) 064301.
[101] P.R. Tulip, S.P. Bates, Mol. Phys. 107 (2009) 2201–2212.
[102] B.Z. Chowdhry, T.J. Dines, S. Jabeen, R. Withnall, J. Phys. Chem. A 112 (2008) 10333–10347.
[103] G. Zheng, S.J. Clark, S. Brand, R.A. Abram, Phys. Rev. B 74 (2006) 165210.
[104] P.U. Jepsen, S.J. Clark, Chem. Phys. Lett. 442 (2007) 275–280.
[105] S.F. Parker, K. Refson, S.M. Tavender, P. Albers, B. Hannebauer, M. Janik, A. Muller, J. Martens, M. Watzke, K. Shankland, C. Leech, H. Offermanns, J. Raman Spectrosc. 40 (2009) 703–708.
[106] S.F. Parker, K. Refson, K.P.J. Williams, D.A. Braden, B.S. Hudson, K. Yvon, Inorg. Chem. 45 (2006) 10951–10957.
[107] L.Y. Lu, D.Q. Wei, X.R. Chen, D. Lian, G.F. Ji, Q.M. Zhang, Z.Z. Gong, Mol. Phys. 106 (2008) 2569–2580.
[108] W. Zhu, X. Zhang, T. Wei, H. Xiao, Theor. Chem. Acc. 124 (2009) 179–186.
[109] W. Zhu, H. Xiao, J. Solid, State Chem. 180 (2007) 3521–3528.
[110] W.H. Zhu, T. Wei, X.W. Zhang, H.M. Xiao, J. Mol. Struct. (THEOCHEM) 895 (2009) 131–137.
[111] J. Tomkinson, J. Riesz, P. Meredith, S.F. Parker, Chem. Phys. 345 (2008) 230–238.
[112] R. Gueta, A. Natan, L. Addadi, S. Weiner, K. Refson, L. Kronik, Angew. Chem. Int. Ed. 46 (2007) 291–294.
[113] Y.Q. Cai, L.T. Zhang, Q.F. Zeng, L.F. Cheng, Y.D. Xu, Solid State Commun. 141 (2007) 262–266.
[114] Y.D. Dai, G.H. Zhao, L.L. Guo, H.X. Liu, Solid State Commun. 149 (2009) 791–794.
[115] Y.D. Dai, G.H. Zhao, H.X. Liu, J. Appl. Phys. 105 (2009) 034111.
[116] C.H. Wang, X.P. Jing, L. Wang, J. Lu, J. Am. Ceram. Soc. 92 (2009) 1547–1551.
[117] J.C. Li, C.L. Wang, M.X. Wang, H. Peng, R.Z. Zhang, M.L. Zhao, J. Liu, J.L. Zhang, L.M. Mei, J. Appl. Phys. 105 (2009) 043503.
[118] H. Wang, J. Zhu, Y.F. Wang, X.W. Cao, M. Feng, G.X. Lan, Physica B 403 (2008) 4189–4195.
[119] C.H. Wang, X.J. Kuang, X.P. Jing, J. Lu, X. Lue, J. Shao, J. Appl. Phys. 103 (2008) 074105.
[120] C.H. Wang, X.P. Jing, W. Feng, J. Lu, J. Appl. Phys. 104 (2008) 034112.
[121] P. Ding, E.J. Liang, Y. Jia, Z.Y. Du, J. Phys.: Condes. Matter 20 (2008) 275224.
[122] E.B. Lombardi, Diamond Relat. Mater. 18 (2009) 835–838.
[123] J.Y. Zhang, L.J. Zhang, T. Cui, Y. Li, Z. He, Y.M. Ma, G.T. Zou, Phys. Rev. B 75 (2007) 104115.
[124] J.Y. Zhang, J.L. Kuo, J. Phys.: Condes. Matter 21 (2009) 015402.
[125] J.I. Tani, H. Kido, Comput. Mater. Sci. 42 (2008) 531–536.
[126] Y.C. Cheng, X.L. Wu, S.H. Li, P.K. Chu, Solid State Commun. 146 (2008) 69–72.
[127] B. Winkler, A. Friedrich, D.J. Wilson, E. Haussuhl, M. Krisch, A. Bosak, K. Refson, V. Milman, Phys. Rev. Lett. 101 (2008) 065501.
[128] A. Bosak, I. Fischer, M. Krisch, V. Brazhkin, T. Dyuzheva, B. Winkler, D. Wilson, D. Weidner, K. Refson, V. Milman, Geophys. Res. Lett. 36 (2009) L19309.
[129] A. Bosak, M. Hoesch, M. Krisch, D. Chernyshov, P. Pattison, C. Schulze-Briese, B. Winkler, V. Milman, K. Refson, D. Antonangeli, D. Farber, Phys. Rev. Lett. 103 (2009) 076403.
[130] Z.Y. Zhang, D.L. Yang, Y.H. Liu, H.B. Cao, J.X. Shao, Q. Jing, Acta Phys. Chim. Sin. 25 (2009) 1731–1736.
[131] D. Zhao, W.D. Cheng, H. Zhang, S.P. Huang, M. Fang, W.L. Zhang, S.L. Yang, J. Mol. Struct. 919 (2009) 178–184.
[132] V.V. Atuchin, Z.S. Lin, L.I. Isaenko, V.G. Kesler, V.N. Kruchinin, S.I. Lobanov, J. Phys.: Condes. Matter 21 (2009) 455502.
[133] J. Hernandez-Paredes, D. Glossman-Mitnik, O. Hernandez-Negrete, H. Esparza-Ponce, M.E. Alvarez, R.R. Mijangos, A. Duarte-Moller, J. Phys Chem. Solids 69 (2008) 1974–1979.
[134] J. Hernandez-Paredes, D. Glossman-Mitnik, H.E. Esparza-Ponce, M.E. Alvarez-Ramos, A. Duarte-Moller, J. Mol. Struct. 875 (2008) 295–301.
[135] M.Z.S. Flores, V.N. Freire, R.P. dos Santos, G.A. Farias, E.W.S. Caetano, M.C.F. de Oliveira, J.R.L. Fernandez, L.M.R. Scolfaro, M.J.B. Bezerra, T.M. Oliveira, G.A. Bezerra, B.S. Cavada, H.W.L. Alves, Phys. Rev. B 77 (2008) 115104.
[136] G.Q. Qin, D.C. Li, Z.J. Feng, S.M. Liu, Thin Solid Films 517 (2009) 3345–3349.
[137] N. Korozlu, K. Colakoglu, E. Deligoz, J. Phys.: Condes. Matter 21 (2009) 175406.
[138] Y.C. Cheng, H.T. Chen, X.X. Li, X.L. Wu, J. Zhu, S.H. Li, P.K. Chu, J. Appl. Phys. 105 (2009) 083511.
[139] C.L. Li, B. Wang, Y.S. Li, R. Wang, J. Phys. D: Appl. Phys. 42 (2009) 065407.
[140] A. Bouhemadou, R. Khenata, F. Djabi, Solid State Sci. 11 (2009) 556–561.
[141] L. He, M.J. Tang, Y. Fang, F.Q. Jing, EPL 83 (2008) 39001.
[142] J. Lin, M.H. Lee, Z.P. Liu, C.T. Chen, C.J. Pickard, Phys. Rev. B 60 (1999) 13380–13389.
[143] M.H. Lee, C.H. Yang, J.H. Jan, Phys. Rev. B 70 (2004) 235110.
[144] Z.S. Lin, J. Lin, Z.Z. Wang, C.T. Chen, M.H. Lee, Phys. Rev. B 62 (2000) 1757–1764.
[145] Z.S. Lin, Z.Z. Wang, C.T. Chen, M.H. Lee, J. Appl. Phys. 90 (2001) 5585–5590.
[146] Z.S. Lin, Z.Z. Wang, C.T. Chen, S.K.Y. Chen, M.H. Lee, J. Appl. Phys. 93 (2003) 9717–9723.
[147] Z. Lin, Z. Wang, C. Chen, S.K. Chen, M.-H. Lee, Chem. Phys. Lett. 367 (2003) 523–527.
[148] L. Bai, Z.S. Lin, Z.Z. Wang, C.T. Chen, M.H. Lee, J. Chem. Phys. 120 (2004) 8772–8778.
[149] L. Bai, Z.S. Lin, Z.Z. Wang, C.T. Chen, J. Appl. Phys. 103 (2008) 083111.
[150] V.V. Atuchin, L.I. Isaenko, V.G. Kesler, S. Lobanov, H. Huang, Z.S. Lin, Solid State Commun. 149 (2009) 572–575.
[151] L.C. Tang, M.H. Lee, C.H. Yang, J.Y. Huang, C.S. Chang, J. Phys.: Condes. Matter 15 (2003) 6043–6055.
[152] Z.S. Lin, Z.H. Wang, C.T. Chen, M.H. Lee, J. Chem. Phys. 118 (2003) 2349–2356.
[153] J.Y. Huang, L.C. Tang, M.H. Lee, J. Phys.: Condes. Matter 13 (2001) 10417–10431.
[154] L.C. Tang, J.Y. Huang, C.S. Chang, M.H. Lee, L.Q. Liu, J. Phys.: Condes. Matter 17 (2005) 7275–7286.
[155] Z.S. Lin, Z.Z. Wang, H.T. Yang, C.T. Chen, M.H. Lee, J. Chem. Phys. 117 (2002) 2809–2813.
[156] Z.S. Lin, Z.Z. Wang, C.T. Chen, I.P. Wu, M.H. Lee, Chem. Phys. Lett. 399 (2004) 125–129.
[157] Y.Z. Tong, X.Y. Meng, Z.Z. Wang, C.T. Chen, M.H. Lee, J. Appl. Phys. 98 (2005) 033504.
[158] J.M. Hu, W.F. Cheng, S.P. Huang, D.S. Wu, Z. Xie, Appl. Phys. Lett. 89 (2006) 261117.
[159] C.F. Sun, C.L. Hu, X. Xu, J.B. Ling, T. Hu, F. Kong, X.F. Long, J.G. Mao, J. Am. Chem. Soc. 131 (2009) 9486–9487.

Please cite this article in press as: V. Milman et al., J. Mol. Struct. (THEOCHEM) (2010), doi:10.1016/j.theochem.2009.12.040